

# Multilayer Mg-pyrophosphate glass ceramic with discontinuous bioactivity. Physicochemical characterization

Nayarit A. Mata<sup>a</sup>, Pablo Velasquez<sup>a</sup>, Angel Murciano<sup>b</sup>, Piedad N. De Aza<sup>a,\*</sup>

<sup>a</sup> Instituto de Bioingeniería, Universidad Miguel Hernández, Avda. Ferrocarril S/n, Elche, Alicante, 03202, Spain

<sup>b</sup> Departamento de Materiales, Óptica y Tecnología Electrónica, Universidad Miguel Hernández, Avda. Universidad S/n, Elche, Alicante, 03202, Spain

## ARTICLE INFO

### Keywords:

A: Sol-gel processes

C: Bioactivity

D: MgO

E: Biomedical applications

## ABSTRACT

Novel pyrophosphate glass ceramic scaffolds (3D-Ca-P<sub>2</sub>) were fabricated and coated with several layers of CaO-P<sub>2</sub>O<sub>5</sub>-SiO<sub>2</sub>-MgO [3D-[Ca/P/Si]-XMg (X = 1,3 and 10 mol%)] as potential bioactive scaffolds for bone regeneration. The core scaffolds present a homogeneous distribution of polygonal grains consisting of 97% Ca<sub>2</sub>P<sub>2</sub>O<sub>7</sub> with CaO-P<sub>2</sub>O<sub>5</sub> glass as the matrix phase. Incorporating MgO into coatings led to extremely porous layers, assembled by nanosized equiaxed particles, which favoured the formation of different phases of tricalcium phosphate instead of pyrophosphate. Possible applications were determined based on Standard ISO/FDIS 23317:2014 for ceramics and powder samples. The 3D-Ca-P<sub>2</sub> scaffolds' non-bioactivity was modulated by coatings of different bioactivity behaviours depending on MgO contents. 3D-[Ca/P/Si]-10Mg was the best scaffold as precipitated hydroxyapatite (HA), was more amorphous than in the other scaffolds because Mg was incorporated into the HA network, which could favour subsequent cell adhesion. The multilayer scaffold provides advantages over others developed until now because in a unique structure all the characteristics required for an implant are combined. On a physical level, mechanical resistance, and porosity, and on a chemical level, a combination of calcium phosphate phases, similar to the mineral phase of bone, doped with Mg ions, which are capable of being transformed into HA in different periods of time.

## 1. Introduction

The incentive of the present work resulted from the authors making longstanding efforts to develop: (i) unconventional CaO-P<sub>2</sub>O<sub>5</sub>-SiO<sub>2</sub> scaffolds as bone substitutes; (ii) the full-bodied synthesis of such biomaterials. Traditionally, CaO-P<sub>2</sub>O<sub>5</sub>-SiO<sub>2</sub> system compositions have been developed as monophasic [1,2], biphasic materials [3,4] and multiphase materials [5,6]. Moreover, the incorporation of silicon into calcium phosphate in an optimal composition can control the material's biodegradability and bioactivity [7,8]. However, the main phases are noticeably orthophosphates, while calcium pyrophosphate (Ca-P<sub>2</sub>) remains relatively unexplored. Pyrophosphate is an essential molecule for the body and is present in plasma, teeth and bone [9–11].

Calcium phosphate solids formation is essentially relevant as calcium phosphate that comes in the calcium hydroxyapatite (HA) form is the main skeletal system constituent. Calcium phosphate deposition in body regions that ought not to calcify takes place under many pathological conditions: e.g., arthritis, bursitis, dental calculus, other ectopic calcification forms, etc. [12]. Several authors have clearly demonstrated the

role of tripolyphosphate, pyrophosphate and long-chain phosphates to inhibit HA formation both *in vitro* and *in vivo* [13,14].

Most of the materials developed show good biocompatibility, but few are developed as three-dimensional scaffolds with excellent physical characteristics such as mechanical strength and porosity. For this reason, our most recent idea was to fabricate a multilayer of stratified materials, where each layer would provide the final material a combination of different requirements. We propose manufacturing a material of non-bioactive behaviour to bioactive, or even intermittent bioactive behaviour, depending on the needs of the implantation site or the patient's health. We hypothesised that by simply modifying the technique used in our above work would lead to a new full-bodied synthesis of CaO-P<sub>2</sub>O<sub>5</sub>-SiO<sub>2</sub> scaffolds consisting of cristobalite, calcium pyrophosphate and different tricalcium phosphate phases as the main phases. An extensive literature search did not detect any previous works along these lines which is, hence, the choice of topic for the present study. Another effort herein made is to assess the possible effects of Mg<sup>2+</sup> as an additive during the synthesis process and on bioactivity behaviour. We have several reasons for choosing Mg<sup>2+</sup>. First of all, Mg<sup>2+</sup> is the fourth most

\* Corresponding author. Instituto de Bioingeniería, Universidad Miguel Hernández, 03202, Elche, Alicante, Spain.

E-mail addresses: [nmata@umh.es](mailto:nmata@umh.es) (N.A. Mata), [pavelasquez@umh.es](mailto:pavelasquez@umh.es) (P. Velasquez), [amurciano@umh.es](mailto:amurciano@umh.es) (A. Murciano), [piedad@umh.es](mailto:piedad@umh.es) (P.N. De Aza).

<https://doi.org/10.1016/j.ceramint.2021.02.044>

Received 19 October 2020; Received in revised form 27 January 2021; Accepted 4 February 2021

Available online 6 February 2021

0272-8842/© 2021 The Authors.

Published by Elsevier Ltd.

This is an open access article under the CC BY-NC-ND license

(<http://creativecommons.org/licenses/by-nc-nd/4.0/>).

abundant ion in the human body, mainly in bones [15]. Secondly,  $Mg^{2+}$  tends to help retain the amorphous phase of calcium phosphates [16]. Thirdly, cell adhesion and proliferation are favoured by amorphous hydroxyapatite [17]. Finally,  $Mg^{2+}$  tends to help stabilise tricalcium phosphate (TCP) as opposed to pyrophosphate [18].

## 2. Materials and methods

In order to obtain pyrophosphate 3D scaffolds (3D-Ca-P<sub>2</sub>), 20 ppi-Polyurethane foams (Eurofoam-Germany-PU) of 13 mm Ø x 10 mm long were coated with a sol-solution composed mainly of: 98% Tetraethyl Orthosilicate, Aldrich (TEOS) as a silicon source; ≥ 99.8% Triethyl Phosphate, Aldrich (TEP) as a phosphorus source; ≥ 99% calcium carbonate, Sigma, as a calcium source. Finally, 99% lithium carbonate, Sigma-Aldrich, was added as a reinforcing agent. In order to obtain an oily solution that was viscous enough to wet the PU foams and would not drip, it was adjusted with 37% hydrochloric acid, Ensure, until pH 2–3, followed by heating for 15 min at 100 °C. Table 1 shows the amount of the different reagents used to obtain the sol-solution. Finally, 30 impregnations of the PU foam in sol-solution were necessary to create a thick enough coating before burning the PU foam and sintering the 3D-Ca-P<sub>2</sub> ceramic at 950 °C/8 h.

In order to improve the bioreabsorption and osteogenesis of the sintered pyrophosphate glass ceramic scaffold, it was coated with silicon and magnesium. New sol-solutions with 1, 3 and 10 mol% MgO were prepared according to Table 1. The 3D-Ca-P<sub>2</sub> ceramic scaffolds were coated 6 times in each new sol-solution and dried at 200 °C for 5 min. Finally, the new 3D-[Ca/P/Si]-XMg-coated scaffolds were sintered at 950 °C/3 h.

Based on Standard ISO/FDIS 23317:2017 for ceramics and powder samples [19], the possible bone tissue repair application of both the 3D-Ca-P<sub>2</sub> scaffolds and 3D-[Ca/P/Si]-XMg coated scaffolds was determined. The 3D scaffolds were immersed in simulated body fluid (SBF) up to 28 days at 37 °C.

The composition and crystalline phases of the manufactured 3D-Ca-P<sub>2</sub> scaffolds and 3D-[Ca/P/Si]-XMg-coated scaffolds were evaluated by X-Ray Diffraction (XRD, Bruker-AXR D8Advance) using Cu-K<sub>α</sub> radiation (1.5418740 Å). Data were collected between 10° and 50° (2θ) at 0.02 steps, counting 8 s per step. The X-Ray tube was operated at 40 kV and 30 mA. Version 3.7.1.132 of Software Match! was used for the Rietveld analysis of diffractograms and the database provided by the Inorganic Crystal Structure Database (ICSD) and the Crystallography Open Database (COD). Next the Fourier-Transform Infrared Spectra (FTIR, Thermo Scientific Nicolet iS5, equipped with iD5 ATR) were collected between 1500 cm<sup>-1</sup> and 450 cm<sup>-1</sup> at a resolution of 4 cm<sup>-1</sup> and room temperature by employing 64 scans.

The physical characterization of the scaffolds was performed on the manufactured 3D-Ca-P<sub>2</sub> and 3D-[Ca/P/Si]-10Mg scaffolds as a representative sample. The porosity and distribution of the pores between 300 μm and 0.004 μm was evaluated by the Mercury Porosimetry Technique using a Poremaster 60 GT Quantachrome instruments, with a pressure between 6.789 kPa and 407,031 kPa. The total porosity of the scaffold was evaluated by pycnometer with water following the Archimedes principle. Compressive strength was evaluated by crushing until rupture with a Microtest SCM3000 instrument. The force was applied axially to the cylindrical scaffolds at a speed of 1.00 mm/min.

The morphology of the uncoated and Mg-coated scaffolds before and

after soaking in SBF was characterised by Scanning Electron Microscopy with Energy Dispersive X-Ray Spectroscopy (SEM-EDX) using a Hitachi S-3500 N and the INCA system by Oxford Instruments Analytical. Scaffolds were electron beam conductive by coating with palladium prior to the SEM study.

To determine the bioactivity and/or biodegradability of the 3D-Ca-P<sub>2</sub> scaffold and 3D-[Ca/P/Si]-XMg-coated scaffolds, changes in the ionic concentration in SBF were established by ICP-OES (inductively-coupled plasma atomic emission spectroscopy; PerkinElmer Optima 2000). Scaffolds were extracted from SBF and examined by SEM-EDX at regular time points.

## 3. Results

The mineralogical study of the 3D-Ca-P<sub>2</sub> and 3D-[Ca/P/Si]-XMg-coated scaffolds after milling displayed several crystalline phases. The XRD pattern of the 3D-Ca-P<sub>2</sub> scaffold (see Fig. 1) displayed the typical peaks in these phases; e.g., cristobalite-SiO<sub>2</sub> (COD 96-900-8225), calcium diphosphate-Ca<sub>2</sub>P<sub>2</sub>O<sub>7</sub> (COD 96-100-1557) and Li(PO<sub>3</sub>) (COD 96-210-7073). The 3D-[Ca/P/Si]-XMg-coated scaffolds showed non-stoichiometric Mg-Tricalcium phosphate (Mg-TCP) Ca<sub>10.115</sub>Mg<sub>0.385</sub>P<sub>7</sub>O<sub>28</sub> (COD 96-901-2137), non-stoichiometric Li-Tricalcium phosphate (Li-TCP) Ca<sub>9.95</sub>Li<sub>1.05</sub>(PO<sub>4</sub>)<sub>7</sub> (COD 96-152-6054) and LiCaPO<sub>4</sub> (COD 96-722-2995). The Rietveld Analysis provided in Table 2 displayed calcium diphosphate from the 3D-Ca-P<sub>2</sub> scaffold as the main phase, followed by non-stoichiometric Mg-TCP in the 3D-[Ca/P/Si]-1Mg and 3D-[Ca/P/Si]-3Mg-coated scaffolds and non-stoichiometric Li-TCP in 3D-[Ca/P/Si]-10Mg.

Fig. 2 depicts the FTIR of the 3D-Ca-P<sub>2</sub> scaffold, along with the spectrum of the 3D-[Ca/P/Si]-10Mg as being representative of all the 3D-[Ca/P/Si]-XMg-coated scaffolds. The Si-O-Si and PO<sub>4</sub><sup>3-</sup> groups overlapped, and the P<sub>2</sub>O<sub>7</sub><sup>4-</sup> and PO<sub>2</sub> groups were present.

The vibration of the PO<sub>4</sub><sup>3-</sup> groups in the scaffolds was denoted by several peaks that grouped in three main zones: (i) asymmetric bending modes by several well-resolved peaks between 526 cm<sup>-1</sup> and 610 cm<sup>-1</sup>; (ii) the symmetric stretching vibration mode by several peaks between 920 cm<sup>-1</sup> and -970 cm<sup>-1</sup>; (iii) the asymmetric stretching vibration mode by another group of several peaks between 1000 cm<sup>-1</sup> and 1084 cm<sup>-1</sup> [20]. According to several studies [21,22], the peak at around 800 cm<sup>-1</sup> was for HPO<sub>4</sub><sup>2-</sup>, which is characteristic of non-stoichiometric calcium phosphates.

The Si-O-Si vibration groups were also found in two main regions: (i) symmetrical stretching or bending, 800–970 cm<sup>-1</sup> and (ii) asymmetrical stretching, 1000–1207 cm<sup>-1</sup>. However, the presence of alkali-earth elements, like magnesium and calcium, modified these structures and a new band that corresponded to Si-O-NBO appeared at 920 cm<sup>-1</sup> [23,24].

The pyrophosphate group (P<sub>2</sub>O<sub>7</sub><sup>4-</sup>) was present and detected by signals at 725 cm<sup>-1</sup>, 920 cm<sup>-1</sup> and 1207 cm<sup>-1</sup> [25] in both scaffolds. Nonetheless, these peaks were much larger in the 3D-Ca-P<sub>2</sub> scaffold.

Finally, the presence of glass in the 3D-Ca-P<sub>2</sub> scaffold was observed by the signals of the PO<sub>2</sub> groups at 1155 cm<sup>-1</sup> asymmetric and 1065 cm<sup>-1</sup> symmetric, and the PO group at 970 cm<sup>-1</sup> and (P=O) at 1280 cm<sup>-1</sup> [26]. All these peaks were much smaller in the coating scaffolds. Moreover, the fact that 1280 cm<sup>-1</sup> disappeared was noteworthy.

The SEM-EDX examination of the microstructure of the 3D-Ca-P<sub>2</sub> and 3D-[Ca/P/Si]-XMg-coated scaffolds is shown in Fig. 3. The 3D-Ca-P<sub>2</sub> scaffolds' microstructure is provided in Fig. 3A–C, which depicts a

**Table 1**  
Chemical composition for manufacturing the glass ceramic and coatings.

	TEP (ml)	TEOS (ml)	CaCO <sub>3</sub> (g)	Li <sub>2</sub> CO <sub>3</sub> (g)	H <sub>2</sub> O (ml)	Ethanol (ml)	HCl (ml)	MgCO <sub>3</sub> (g)
3D-Ca-P <sub>2</sub>	10	0.5	8	0.5	20	5	10	-
3D-[Ca/P/Si]-1Mg	1.6	11	11.2	-	20	5	10	0.1
3D-[Ca/P/Si]-3Mg	1.6	11	11	-	20	5	10	0.3
3D-[Ca/P/Si]-10Mg	1.6	11	10	-	20	5	10	1.0

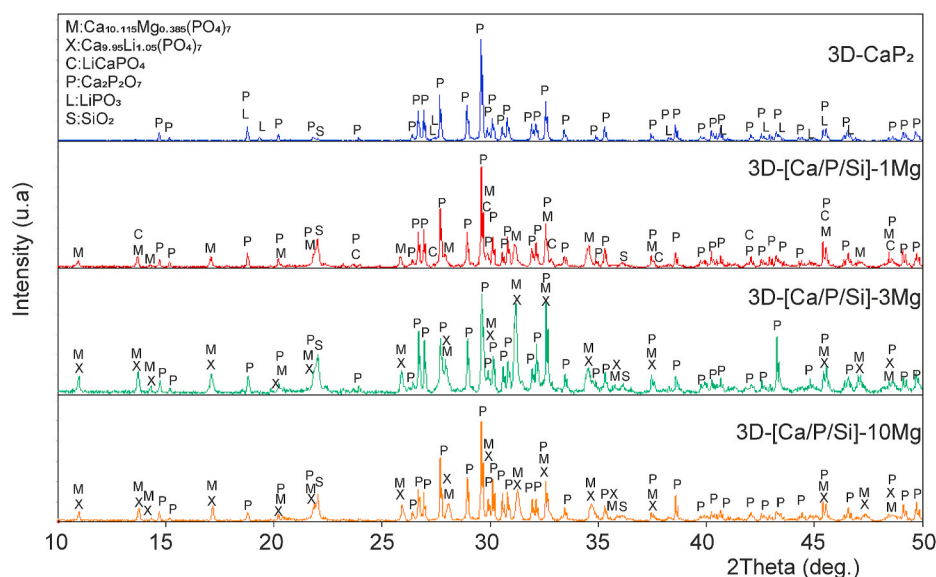


Fig. 1. XRD of the 3D-Ca-P<sub>2</sub> and 3D-[Ca/P/Si]-XMg-coated scaffolds.

Table 2  
Rietveld analysis.

Sample	Phase (%)	$\chi^2$
3D-Ca-P <sub>2</sub>	Ca <sub>2</sub> P <sub>2</sub> O <sub>7</sub>	97.1
	Li(PO <sub>3</sub> )	1.7
	SiO <sub>2</sub>	1.1
3D-[Ca/P/Si]-1Mg	Ca <sub>2</sub> P <sub>2</sub> O <sub>7</sub>	61.3
	Ca <sub>10.115</sub> Mg <sub>0.385</sub> P <sub>7</sub> O <sub>28</sub>	19.3
	SiO <sub>2</sub>	14.2
	LiCa(PO <sub>4</sub> )	4.5
3D-[Ca/P/Si]-3Mg	Ca <sub>2</sub> P <sub>2</sub> O <sub>7</sub>	57.5
	Ca <sub>10.115</sub> Mg <sub>0.385</sub> P <sub>7</sub> O <sub>28</sub>	29.7
	Ca <sub>9.95</sub> Li <sub>1.05</sub> (PO <sub>4</sub> ) <sub>7</sub>	7
	SiO <sub>2</sub>	5.8
3D-[Ca/P/Si]-10Mg	Ca <sub>2</sub> P <sub>2</sub> O <sub>7</sub>	58.6
	Ca <sub>9.95</sub> Li <sub>1.05</sub> (PO <sub>4</sub> ) <sub>7</sub>	27
	Ca <sub>10.115</sub> Mg <sub>0.385</sub> P <sub>7</sub> O <sub>28</sub>	8.7
	SiO <sub>2</sub>	5.6

highly porous structure (porosity ~ 70% and pore size ~400–700  $\mu\text{m}$ ) obtained by the sol-gel processing route. Fig. 3A depicts a low-magnification microstructure of the 3D-Ca-P<sub>2</sub> scaffolds. At increasing magnification, a microstructure, performed by the homogeneous distribution of polygonal grains with  $0.93 < \text{Ca/P} < 1.06$ , was distinguished and came very close to the Ca/P ratio of the main phase in the Rietveld analysis (97% of Ca<sub>2</sub>P<sub>2</sub>O<sub>7</sub>). Bordering these polygonal crystals appeared a glassy phase, mainly in triple points (arrows in Fig. 3B and C), with a  $0.25 < \text{Ca/P} < 0.35$  ratio. The XRD did not show the typical broadband when glass is present in material. So the amorphous glass phase was not enough to be detected by the XRD, but conferred the scaffold a whitish vitreous appearance.

Fig. 3D–F shows the 3D-[Ca/P/Si]-XMg-coated scaffolds' microstructure. As magnesium content increase, the coated layers became bigger and covered a larger surface of the 3D-Ca-P<sub>2</sub> scaffolds. The coated layers related to non-stoichiometric Mg-TCP and the Li-TCP phases were found to be extremely porous materials, which were assembled by nanosized equiaxed particles (Fig. 3G). The EDX results revealed that Mg content only came to 25% of (Ca + Mg). The Ca/P or (Ca + Mg)/P ratio in the 3D-[Ca/P/Si]-XMg-coated scaffolds respectively came close to 1 and 1.5, which matched the chemical formulae of Ca<sub>2</sub>P<sub>2</sub>O<sub>7</sub> from the

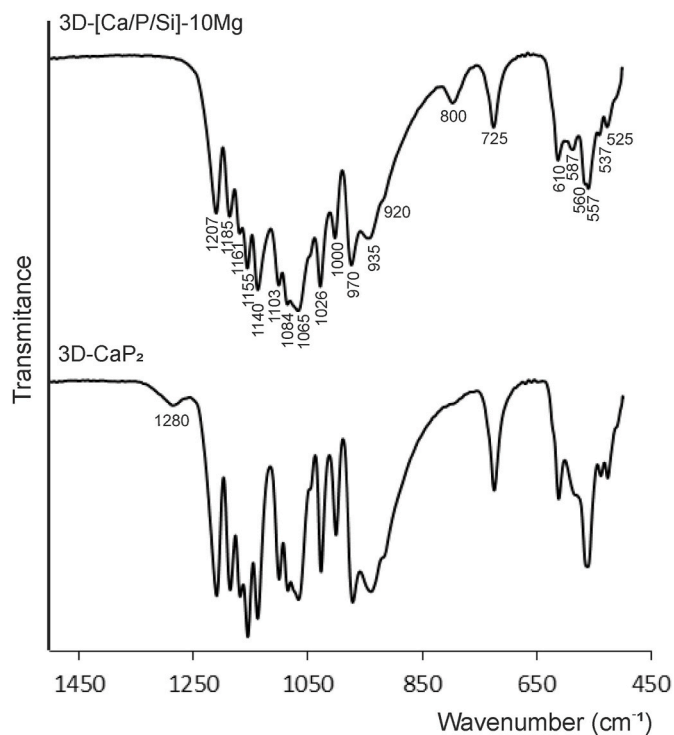


Fig. 2. The ATR-FTIR spectra of the 3D-Ca-P<sub>2</sub> scaffold and 3D-[Ca/P/Si]-10Mg as being representative of all the coated scaffolds.

bottom scaffold and those of Ca<sub>10.115</sub>Mg<sub>0.385</sub>P<sub>7</sub>O<sub>28</sub> from the coating. The Li<sup>+</sup> content in the 3D-[Ca/P/Si]-XMg coatings was negligible as it went below the limit of detection for SEM.

Fig. 4 shows the results obtained by Mercury Porosimetry Technique. According to the volume of the intruded mercury, the curves show (Fig. 4A–B) that the uncoated scaffold (3D-Ca-P<sub>2</sub>) had a greater number of intraparticle pores, with a pore distribution of approximately 0.1  $\mu\text{m}$ –0.004  $\mu\text{m}$ , and less interparticle pores between 200  $\mu\text{m}$  and 10  $\mu\text{m}$ . On the contrary, this same sample, but now coated (3D-[Ca/P/Si]-10Mg), presented mostly interparticle pores, with two important ranges of intruded mercury. The first of these ranges was between 200  $\mu\text{m}$  and 35  $\mu\text{m}$  and the second between 33  $\mu\text{m}$  and 4.5  $\mu\text{m}$ . Table 3 shows the

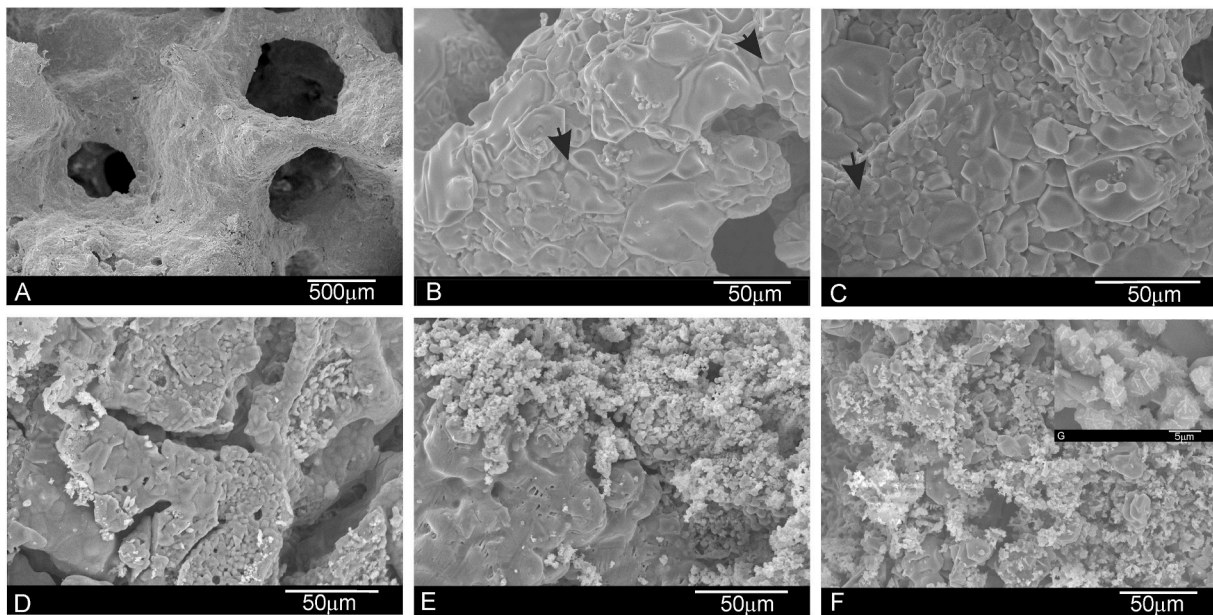


Fig. 3. SEM micrographs of the 3D-Ca-P<sub>2</sub> (A–C) and 3D-[Ca/P/Si]-XMg-coated scaffolds with 1 mol%Mg (D), 3 mol%Mg (E) and 10 mol%Mg (F) [arrows in B and C denote the glass phase].

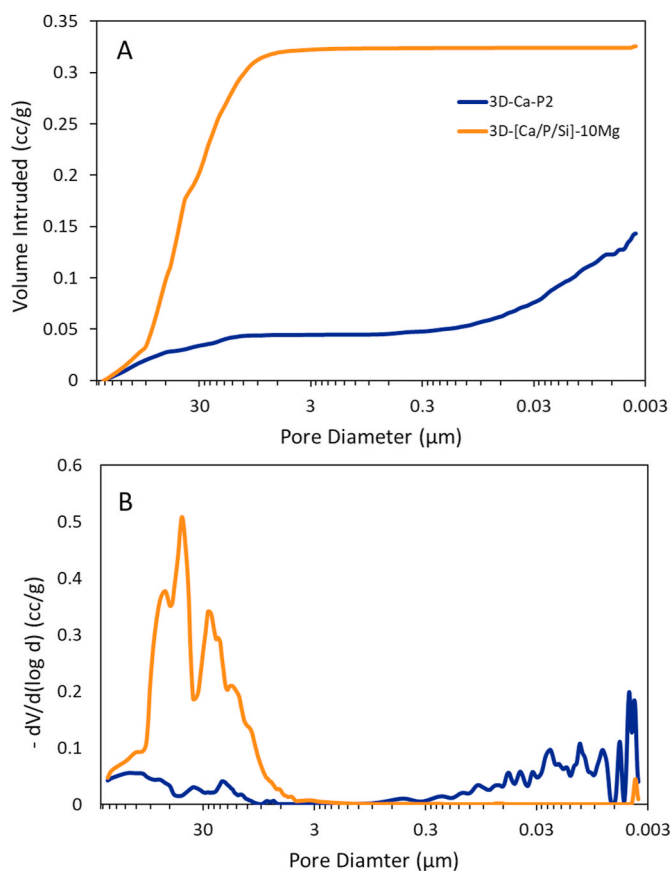


Fig. 4. Mercury porosimetry curves of the 3D-Ca-P<sub>2</sub> and 3D-[Ca/P/Si]-10Mg scaffold. (A) differential and (B) cumulative volume intruded versus pore diameter.

percentages of both types of pores as well as other physical properties of these scaffolds. The total porosity of the material network was 23.76% for sample 3D-Ca-P<sub>2</sub> and 49.50% for sample 3D-[Ca/P/Si]-10Mg. The

porosity of the scaffolds and compressive strength were 42% and 2.87 MPa for 3D-Ca-P<sub>2</sub> scaffold and 34% and 3.38 MPa for 3D-[Ca/P/Si]-10Mg scaffold.

Figs. 5 and 6 show the surface morphology changes of the 3D-Ca-P<sub>2</sub> and 3D-[Ca/P/Si]-XMg-coated scaffolds, respectively, after being soaked in SBF for different times.

No morphological changes were observed at the beginning of the assay in the 3D-Ca-P<sub>2</sub> microstructure (Fig. 5A). After 7 soaking days, the polygonal grains of calcium diphosphate appeared to be more individualised due to glass phase degradation (Fig. 5B). After 21 soaking days, the polygonal grains had rounded edges and the glass phase did not completely dissolve as the 3D structure remained throughout the test (Fig. 5C). At high magnification, the polygonal grains were glued by the rest of glass phase that acts a bonding agent. A small white precipitate, composed mainly of silicon, was also observed sporadically after 28 testing days (Fig. 5D).

After 3 soaking days, the morphology of the 3D-[Ca/P/Si]-1Mg-coated scaffolds completely differed from the original one (Fig. 1D). A dense spherical precipitate layer coated the whole scaffold surface which, at high magnification, was formed by needle-like crystals. The EDX analysis revealed that these spherical precipitates gave 1.36 < Ca/P < 1.50. After 7 and 14 soaking days, the new spherical layer seemed to disappear. At low magnification, the image taken on day 7 revealed the bottom 3D-Ca-P<sub>2</sub> microstructure with some minor remains of the precipitate dispersed on the surface. Details of the remaining phase were observed at high magnification on day 7. On day 21, the surface was once again coated with a spherical precipitate. At high magnification, it was formed by needle-like crystallites. The EDX done of the spherical precipitate on day 21 gave 1.11 < Ca/P < 1.39 or 1.15 < (Ca + Mg)/P < 1.46, and 1.30 < Ca/P < 1.44 or 1.40 < (Ca + Mg)/P < 1.54 on day 28. At 14 and 21 days, small conglomerates of white cauliflower-like precipitates were dispersed on the surface (arrow for days 14 and 21). EDX indicated a composition made up mainly of silicon. On day 28, the new precipitate's morphology did not change.

On soaking days 3 and 7, the 3D-[Ca/P/Si]-3Mg-coated scaffolds' morphology showed polygonal grains of the calcium diphosphate from the 3D-Ca-P<sub>2</sub> scaffold, together with some remains of the 3D-[Ca/P/Si]-3Mg coating scattered on the scaffold surface. After 14 soaking days, morphology drastically changed with the appearance of a new spherical precipitate coating with 1.23 < Ca/P < 1.31 or 1.33 < (Ca + Mg)/P <

**Table 3**  
Summary of the physical characterization of the scaffolds.

Sample	Interparticle Porosity (%) <sup>a</sup>	Intraparticle Porosity (%) <sup>b</sup>	Total Porosity Network (%)	Apparent Density Network (g/cc)	Scaffold Porosity (%)	Compressive strength (MPa)
3D-Ca-P <sub>2</sub>	7.38	16.38	23.76	1.66	42	2.87
3D-[Ca/P/Si]-10Mg	48.85	0.65	49.50	1.52	34	3.38

<sup>a</sup> Corresponding to pores between 1 μm–300 μm.

<sup>b</sup> Corresponding to pores <1 μm.

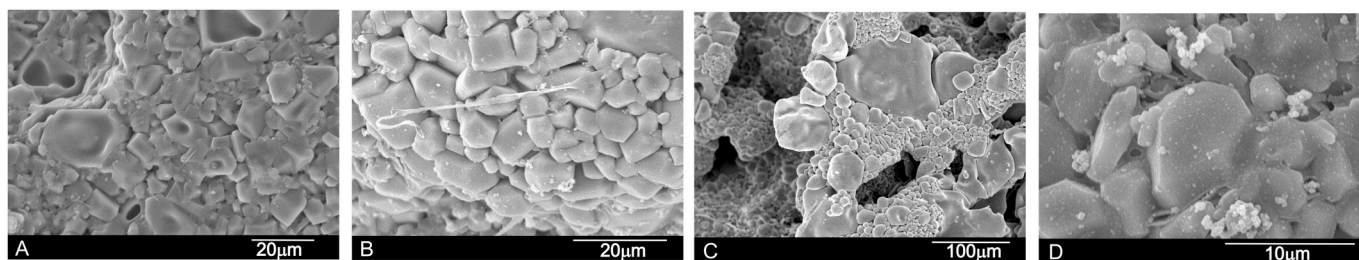


**Fig. 5.** SEM micrographs of the 3D-Ca-P<sub>2</sub> scaffolds after (A) 3 days, (B) 7 days, (C) 21 days and (D) 28 days of SBF soaking.

1.36. On day 21, the spherical precipitate coating neither seemed as dense as the 14-day precipitate, nor formed a continuous layer on the entire surface. At the end of the 28-day soaking time, the spherical precipitate formed again. Although it still did not cover the whole surface, it seemed denser than the 21-day layer. A lamellar microstructure was observed beneath the new precipitate given the partial dissolution of the glass from the 3D-Ca-P<sub>2</sub> scaffold (28 days, inner).

After 3 and 7 soaking days, the 3D-[Ca/P/Si]-10Mg-coated scaffold showed a similar microstructure to the 3D-[Ca/P/Si]-3Mg scaffold and at the same soaking time. This indicated the grains of the 3D-Ca-P<sub>2</sub> scaffold with rounded edges given their partial dissolution and the dissolution of the glass phase. Sporadically, part of the coating remained on the rounded calcium pyrophosphate grains. After 14 and 21 days of soaking, a dense globular precipitate layer coated the scaffold surface which, at high magnification, had a cotton-like morphology. The EDX analysis revealed that these globular precipitates had  $1.18 < \text{Ca/P} < 1.21$  or  $1.21 < (\text{Ca} + \text{Mg})/\text{P} < 1.31$ . At the end of the soaking time, the new globular precipitate had partially dissolved to reveal rounded grains beneath the 3D-Ca-P<sub>2</sub> scaffold.

The ion changes in SBF, due to the different scaffolds' behaviours after several soaking times in SBF, are presented in Fig. 7. We can see that the behaviour of the calcium, phosphorous and silicon ions vastly differed depending on the scaffold type being tested.

The 3D-Ca-P scaffolds showed calcium ion adsorption from SBF as it was depleted in the surrounding medium. Phosphorous ions were released from the scaffold to SBF. Finally, the silicon ion concentration did not change while the study was underway.

In contrast, the changes in the 3D-[Ca/P/Si]-XMg-coated scaffolds were more drastic and sinusoidal behaviour was noted throughout the trial. For the 3D-[Ca/P/Si]-XMg scaffold, silicon and phosphorous behaviours displayed the inverse behaviour when the silicon concentration rose and the phosphorus one lowered, except at the beginning of the trial (day 3), when P rose in 3D-[Ca/P/Si]-3Mg and slightly lowered in 3D-[Ca/P/Si]-10Mg.

#### 4. Discussion

The 3D-Ca-P<sub>2</sub> scaffolds were obtained by immersing polyurethane foams in sol-solutions followed by heat treatment [27]. In order to obtain a 3D material consisting of Ca<sub>2</sub>P<sub>2</sub>O<sub>7</sub> crystals, crystals should be dispersed in a matrix phase. Ca<sub>2</sub>P<sub>2</sub>O<sub>7</sub> crystals reinforced with CaO-P<sub>2</sub>O<sub>5</sub>

glass matrix materials are believed to be good candidates for developing 3D scaffolds with excellent mechanical strength, because viscosity and proportion of glass phase, at the desired temperature, vary with composition [28]. According to the CaO-P<sub>2</sub>O<sub>5</sub> phase diagram, Ca<sub>2</sub>P<sub>2</sub>O<sub>7</sub> firstly presents the appearance of the liquid phase at 950 °C [29]. For this reason, the 3D material consisted of Ca<sub>2</sub>P<sub>2</sub>O<sub>7</sub> crystals, in which a small amount of CaO-P<sub>2</sub>O<sub>5</sub> glass was intentionally prepared. The 3D-Ca-P<sub>2</sub> scaffold had a vitreous appearance related to the glass phase, which was not enough to detect a broadband in XRD, and its presence was determined by the 155 cm<sup>-1</sup>, 1065 cm<sup>-1</sup> and 970 cm<sup>-1</sup> signals in FTIR [26] (Fig. 2).

3D-Ca-P<sub>2</sub> scaffold densification took place during heating, with a maximum shrinkage of ~30%. Glass acted as a bonding agent to interlink the Ca<sub>2</sub>P<sub>2</sub>O<sub>7</sub> polygonal crystals in the 3D-Ca-P<sub>2</sub> scaffold (Fig. 2B and C). The glass phase did not crystallise upon cooling. The final microstructure comprised grains with a broad size distribution ranging from relatively small (10–15 μm) to quite large (70–75 μm). The microstructure reflected the liquid-phase sintering process by the dissolution/crystallization mechanism, when bigger grains further enlarged and smaller grains were dissolved during the CaO-P<sub>2</sub>O<sub>5</sub> melt. The XRD pattern of the milled 3D-Ca-P<sub>2</sub> scaffold after sintering included 97.1% Ca<sub>2</sub>P<sub>2</sub>O<sub>7</sub>, 1.7% Li(PO<sub>3</sub>) and 1.1% cristobalite (Table 2).

The 3D-Ca-P<sub>2</sub> scaffolds were coated with 3D-[Ca/P/Si]-XMg and developed a scaffold with a high porous coatings. The porosity of the coatings was verified with the curves in Fig. 4 and the data reported in Table 3. The intra- and interparticle porosity is the total microporosity of the scaffolds (pores < 300 μm) and for the 3D-[Ca/P/Si]-10Mg scaffold it was much higher compared to the same uncoated scaffold as a consequence of the superficial change observed between both (Fig. 3). The 3D-Ca-P<sub>2</sub> scaffold originally had mostly intraparticle pores and by coating it with the second composition the interparticle pores increased. At macro level (pores > 300 μm), the opposite happened, the decrease of the total porosity of the 3D-Ca-P<sub>2</sub> scaffold with respect to the 3D-[Ca/P/Si]-10Mg scaffold was due to the fact that the coatings made on the porous scaffold reduced the diameter of the big pores originally found in the polyurethane sponge. The presence of submicron and nanosized pores gives the scaffold excellent characteristics for future applications. This means they can be suitably used as both bone substitutes and bimolecular carriers [30]. Although there is no consensus on the ideal pore size of a scaffold, both macro- and microporosity are necessary. According to Rustom et al. pores larger than 100 μm are required for

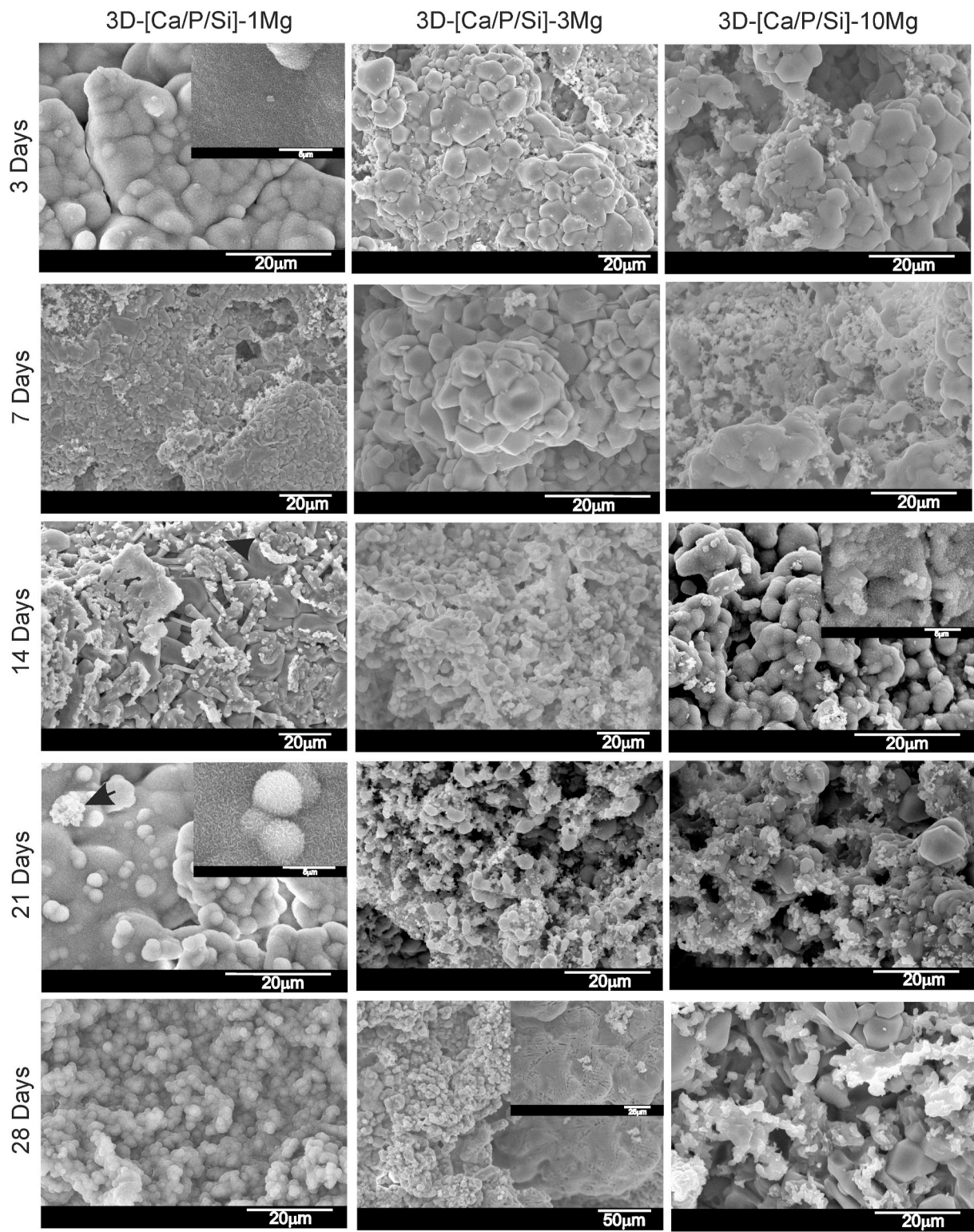


Fig. 6. SEM micrographs of the 3D-[Ca/P/Si]-XMg-coated scaffolds after different soaking times in SBF.

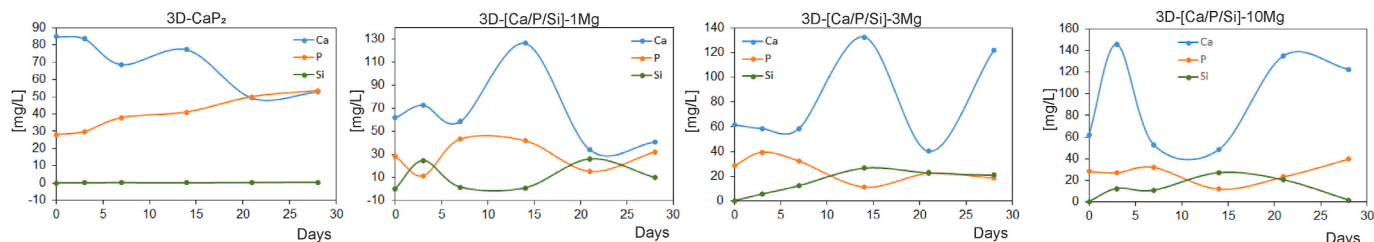


Fig. 7. Ion concentration changes in SBF during the soakings of the 3D-Ca-P<sub>2</sub> and 3D-[Ca/P/Si]-XMg-coated scaffolds.

bone growth, but also pores smaller than 50  $\mu\text{m}$  because they provide additional spaces for bone growth and contribute to the improvement of mechanical strength as a result of filling those spaces [31].

The compression strength of the 3D-Ca-P<sub>2</sub> scaffold was high but increased with the coatings. This is due to the reduced macroporosity presented by the 3D-[Ca/P/Si]-10Mg scaffolds. However, despite the decrease, both scaffolds showed a compressive strength comparable to trabecular or spongy bone. According to Caeiro et al., depending on the region of the skeleton, the compressive strength of the trabecular bone varies between 1.5 and 9.3 MPa [32]. While Gibson et al., presented a compressive strength between 0.2 and 4 MPa when the relative density is around 0.1 [33].

Given the EDX and XRD results, the 3D-[Ca/P/Si]-XMg scaffolds included the Ca<sub>2</sub>P<sub>2</sub>O<sub>7</sub> and SiO<sub>2</sub> phases of the 3D-Ca-P<sub>2</sub> scaffold, plus Ca<sub>10.115</sub>Mg<sub>0.385</sub>P<sub>7</sub>O<sub>28</sub>, Ca<sub>9.95</sub>Li<sub>1.05</sub>(PO<sub>4</sub>)<sub>7</sub>, and LiCaPO<sub>4</sub>. The different TCP-containing phases increased as the sol-solution rose from 1 mol% Mg to 10 mol% Mg. (Fig. 1, Table 2). The Mg<sup>2+</sup> with an ionic radius (0.65 Å) smaller than Ca<sup>2+</sup> (0.99 Å) allowed Ca<sup>2+</sup> to be replaced with Mg<sup>2+</sup> in TCP. The EDX results indicated that Mg<sup>2+</sup> content only amounted to 25% of (Ca + Mg). This finding agrees with Zhou et al. [34], who reported up to 22% Mg<sup>2+</sup> of Ca<sup>2+</sup> replacement in calcium pyrophosphate, and agrees with Yasukawa et al. [35], who reported 30% Mg<sup>2+</sup>.

When the Ca<sup>2+</sup> and Mg<sup>2+</sup> contents from the 3D-[Ca/P/Si]-XMg sol-solution increased, two processes occurred at the same time: (i) part of the glass began to dissolve (the FTIR peaks related to the glass phase were much smaller; Fig. 2), and reacted with the coating to give rise to new Li<sup>+</sup> phases; (ii) the Ca<sub>2</sub>P<sub>2</sub>O<sub>7</sub> phase started to transform into TCP (Ca/P increased from 1 to ~1.5). So that Ca<sup>2+</sup> and Mg<sup>2+</sup> concentrations rose, the Ca<sub>2</sub>P<sub>2</sub>O<sub>7</sub> phase decreased and the non-stoichiometric-TCP phases increased, as observed in the Rietveld analysis of the 3D-[Ca/P/Si]-XMg scaffolds (Table 2). The formation kinetics of the highly porous coat (Fig. 3D–G) is complex and unclear. It has been suggested that the formation of a nano-sized equiaxed crystals structure from the coating is related to a battle of free Ca<sup>2+</sup> and Mg<sup>2+</sup> to bind to PO<sub>4</sub><sup>3-</sup>. This battle between Ca<sup>2+</sup> and Mg<sup>2+</sup> ions has been reported by several authors, who describe how, depending on the type/s of calcium phosphate phase/s present in the material, needle-like and plate-like particles [36],

and even amorphous spheres [37,38], can be generated. The 3D-Ca-P<sub>2</sub> scaffolds presented no bioactivity at any assay time point. The 3D-[Ca/P/Si]-XMg-coated scaffolds displayed intermittent bioactivity, which meant that the amount of Mg-dopant modified scaffolds' *in vitro* behaviour. Fig. 8 shows a summary of the different bioactivity kinetics of the glass-ceramics studied.

The non-bioactive behaviour of pyrophosphate is well-documented given the presence of P<sub>2</sub>O<sub>7</sub><sup>4-</sup> groups that inhibit hydroxyapatite precipitation [39–41]. Conversely, all the 3D-[Ca/P/Si]-XMg scaffolds exhibited intermittent bioactivity at different testing times. What they all have in common is that when there is an incorporation of silicon and decrease in phosphorus into the medium, HA precipitation occurs (Figs. 5 and 6). For example, on days 3, 21 and 28 in the 3D-[Ca/P/Si]-1Mg scaffolds; on days 14 and 28 in the 3D-[Ca/P/Si]-3Mg scaffolds; on days 14 and 21 in the 3D-[Ca/P/Si]-10Mg scaffolds (Figs. 5 and 6). On the contrary, when P increases and Si decreases in the medium, the dissolution of HA takes place (HA previously precipitated on scaffold surfaces), and starts to precipitate to a phase rich in Si (probably Si-OH) by generating possible anchor points on the surface so that the new HA precipitate can nucleate and grow. This was seen on days 7 and 14 in the 3D-[Ca/P/Si]-1 Mg scaffolds; on day 21 in the 3D-[Ca/P/Si]-3 Mg scaffolds; on day 28 in the 3D-[Ca/P/Si]-10 Mg scaffolds. Some remains of the previously precipitated HA layer were observed on the scaffolds, together with a new white silicon-rich precipitate (34.22 > Si > 1.89). The polygonal grains from the 3D-Ca-P<sub>2</sub> scaffold were visible underneath.

In order to explain the dissolution of the HA precipitate layer in scaffolds, it is necessary to contemplate the dissolution of glass. The glass presents in the material that came into contact with SBF was hydrolysed and produced the dissolution of the glass phase of the 3D-Ca-P<sub>2</sub> scaffold by releasing groups (P<sub>2</sub>O<sub>7</sub><sup>4-</sup>) to the medium. The chelating effect of polyphosphates present in glasses on divalent cations is well-known [42], which can react vigorously with the Ca<sup>2+</sup> of the precipitated HA to break the crystalline structure of (Ca<sub>10</sub>(PO<sub>4</sub>)<sub>6</sub>(OH)<sub>2</sub>). As far as we know, this is the first bioactivity mechanism based on the competitive process between a core generator of pyrophosphate and the coating source of HA.

The incorporation of Mg into the HA network leads to HA precipitate crystallinity. This network distortion is not so marked for low Mg<sup>2+</sup> concentrations and, consequently, HA is more crystalline (3D-[Ca/P/Si]-1 Mg at 21 days) than for high Mg<sup>2+</sup> concentrations, where HA is more amorphous (3D-[Ca/P/Si]-10 Mg at 14 days). This favours subsequent cell adhesion because cells are favoured by amorphous HA, as in human bone, than with crystalline HA [43].

The scaffold obtained in this study stands out for (i) having a multilayer structure that allowed combining the benefits of two different chemical compositions, (ii) presenting a core mainly constituted by the calcium pyrophosphate phase, which inhibits the crystallization of HA *in vitro*, but provides mechanical resistance and (iii) presenting external coatings that provided bioactivity, with magnesium ions that improve cell adhesion.

These three characteristics allowed the scaffold to present a bioactivity mechanism promoted by the vitreous phase of the core and the external layers. In addition, depending on the magnesium

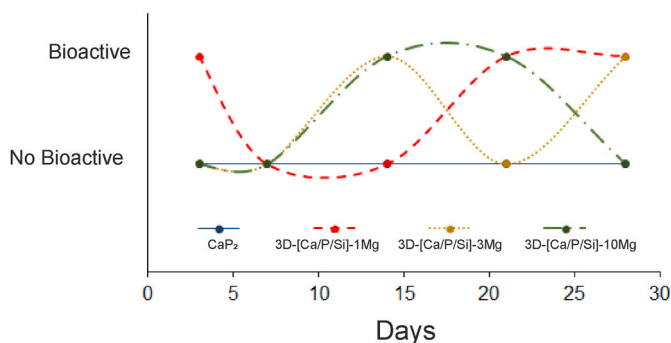


Fig. 8. Bioactivity kinetics of the 3D-Ca-P<sub>2</sub> scaffold and 3D-[Ca/P/Si]-XMg coated scaffolds.

concentration, the HA precipitate was formed at different times and with different morphologies.

In general, the scaffold presents characteristics difficult to obtain in a single structure such as mechanical resistance, porosity and modulated bioactivity.

## 5. Conclusions

Novel pyrophosphate glass ceramic scaffolds containing polygonal grains of calcium pyrophosphate with CaO-P<sub>2</sub>O<sub>5</sub> glass as the matrix phase were manufactured and coated with several CaO-SiO<sub>2</sub>-MgO [3D-[Ca/P/Si]-XMg (X = 1, 3 and 10 mol%)] layers by sol-gel and the polymer replication method. The core of multilayer scaffold provided a three-dimensional structure with mechanical resistance and porosity to support the external coatings that provided the bioactivity.

We were able to modulate scaffolds' bioactivity from a non-bioactive material like the 3D-Ca-P<sub>2</sub> core to scaffolds with intermittent bioactivity depending on the coating's magnesium content. Of all the coated scaffolds that we prepared, in our view that with the best bioactivity was 3D-[Ca/P/Si]-10Mg because the formed HA was more amorphous due to the incorporation of Mg<sup>2+</sup> into the HA lattice. This made the precipitated HA similar to the biological HA of human bone, which would allow cells to adhere better. This means that we can produce materials according to the specific needs of each application.

## Declaration of competing interest

The authors declare that they have no known competing financial interests or personal relationships that could have appeared to influence the work reported in this paper.

## Acknowledgements

The Ph.D. student Nayarit A. Mata has been funded by a grant from the Government of Generalitat Valenciana with reference GRISOLIAP/2018/037.

## References

- [1] S. Xu, Q. Wu, Y. Guo, C. Ning, K. Dai, Copper containing silicocarnotite bioceramic with improved mechanical strength and antibacterial activity, *Mater. Sci. Eng. C* 118 (2021) 111493, <https://doi.org/10.1016/j.msec.2020.111493>.
- [2] G. Dong, Y. Zheng, L. He, G. Wu, C. Deng, The effect of silicon doping on the transformation of amorphous calcium phosphate to silicon-substituted  $\alpha$ -tricalcium phosphate by heat treatment, *Ceram. Int.* 42 (1) (2016) 883–890, <https://doi.org/10.1016/j.ceramint.2015.09.013>. Part A.
- [3] S. Ramezani, R. Emadi, M. Kharazilha, F. Tavangarian, Synthesis, characterization and in vitro behavior of nanostructured diopside/biphase calcium phosphate scaffolds, *Mater. Chem. Phys.* 186 (2017) 415–425, <https://doi.org/10.1016/j.matchemphys.2016.11.013>.
- [4] B. Jokic, I. Stamenkovic, M. Zrilic, K. Obradovic-Djuricic, R. Petrovic, D. Janackovic, Silicon-doped biphasic  $\alpha$ -calcium-phosphate/hydroxyapatite scaffolds obtained by a replica foam method using uniform pre-annealed spherical particles, *Mater. Lett.* 74 (2012) 155–158, <https://doi.org/10.1016/j.matlet.2012.01.081>.
- [5] S. Hesaraki, H. Nazarian, M. Alizadeh, Multi-phase biocomposite material in-situ fabricated by using hydroxyapatite and amorphous nanosilica, *Int. J. Mater. Res.* 102 (5) (2011) 494–503, <https://doi.org/10.3139/146.110397>.
- [6] N.A. Mata, P. Ros-Tàrraga, P. Velasquez, A. Murciano, P.N. De Aza, Synthesis and Characterization of 3D multilayer porous Si-Ca-P scaffolds doped with Sr ions to modulate in vitro bioactivity, *Ceram. Int.* 46 (1) (2020) 968–977, <https://doi.org/10.1016/j.ceramint.2019.09.058>.
- [7] J.H. Shepherd, D.V. Shepherd, S.M. Best, Substituted hydroxyapatites for bone repair, *J. Mater. Sci. Mater. Med.* 23 (2012) 2335–2347, <https://doi.org/10.1007/s10856-012-4598-2>.
- [8] A.V. Zanfiri, N. Nenu, G. Voicu, A.I. Badanoiu, C.D. Ghitulica, F. Iordache, Modified calcium silicophosphate cements with improved properties, *Mater. Chem. Phys.* 238 (1) (2019) 121965, <https://doi.org/10.1016/j.matchemphys.2019.121965>.
- [9] I.S. Kulaev, V. Vagabov, T. Kulakovskaya, *The Biochemistry of Inorganic Polyphosphates*, second ed., John Wiley, Chichester, 2004.
- [10] A. Kornberg, N.N. Rao, D. Ault-Riché, Inorganic polyphosphate: a molecule of many functions, *Annu. Rev. Biochem.* 68 (1999) 89–125, <https://doi.org/10.1146/annurev.biochem.68.1.89>.
- [11] *Inorganic polyphosphates; biochemistry, biology, biotechnology*, in: H.C. Schröder, W.E.G. Müller (Eds.), *Progress in Molecular and Subcellular Biology*, vol. 23, Springer Verlag, Berlin, 1999.
- [12] R.A. Terkeltaub, Inorganic pyrophosphate generation and disposition in pathophysiology, *Am. J. Physiol. Cell Physiol.* 281 (1) (2001) C1–C11, <https://doi.org/10.1152/ajpcell.2001.281.1.C1>.
- [13] H. Fleisch, R.G.G. Russell, F. Straumann, Effect of pyrophosphate on hydroxyapatite and its implications in calcium homeostasis, *Nature* 212 (23) (1966) 901–903.
- [14] R.G. Russell, R.C. Muhlbauer, S. Bisaz, D.A. Williams, H. Fleisch, The influence of pyrophosphate, condensed phosphates, phosphonates and other phosphate compounds on the dissolution of hydroxyapatite in vitro and on bone resorption induced by parathyroid hormone in tissue culture and in thyroparathyroidectomized rats, *Calcif. Tissue Res.* 6 (1970) 183–196, <https://doi.org/10.1007/BF02196199>.
- [15] W. Jahnhen-Dechent, M. Ketteler, Magnesium basics (suppl1), i3–i14, *Clin. Kidney J.* (2012) 5, <https://doi.org/10.1093/ndtplus/sfr163>.
- [16] M. Supová, Substituted hydroxyapatites for biomedical applications: a review, *Ceram. Int.* 41 (8) (2015) 9203–9231, <https://doi.org/10.1016/j.ceramint.2015.03.316>.
- [17] A. Gozalian, A. Behnamghader, M. Daliri, A. Moshkforoush, Synthesis and thermal behavior of Mg-doped calcium phosphate nanopowders via the sol gel method, *Sci. Iran.* 18 (2011) 1614–1622, <https://doi.org/10.1016/j.scient.2011.11.014>.
- [18] P.M.C. Torres, J.C.C. Abrantes, A. Kaushal, S. Pina, N. Döbelin, M. Bohner, J.M. F. Ferreira, Influence of Mg-doping, calcium pyrophosphate impurities and cooling rate on the allotropic  $\alpha$ - $\beta$ -tricalcium phosphate phase transformations, *J. Eur. Ceram. Soc.* 36 (2016) 817–827, <https://doi.org/10.1016/j.jeurceramsoc.2015.09.037>.
- [19] ISO/FDIS 23317, *Implants for Surgery- in Vitro Evaluation for Apatite-Forming Ability of Implant Materials*, 2007.
- [20] P.N. De Aza, F. Guitian, C. Santos, S. De Aza, R. Cusco, L. Artus, Vibrational properties of calcium phosphate compounds. II comparison between hydroxyapatite and  $\beta$ -tricalcium phosphate, *Chem. Mater.* 9 (1997) 916–922, <https://doi.org/10.1021/cm9604266>.
- [21] L. Berzina-Cimdina, N. Borodajenko, Research of calcium phosphates using Fourier transform infrared spectroscopy, *Infrared Spectroscopy-Materials Science, Engineering and Technology* 12 (7) (2012 Apr 25) 251–263.
- [22] A.R. Toibah, I. Sopyan, Y.M. Yuhazri, R.A. Jeefferie, O. Nooririnah, FTIR study on phase behavior of magnesium-doped biphasic calcium phosphate synthesized via sol-gel method, in: *InAIP Conference Proceedings* 2nd, vol. 1455, American Institute of Physics, 2012 Jun 29, pp. 97–103, <https://doi.org/10.1063/1.4732476>. No. 1.
- [23] H. Aguiña, J. Serra, P. Gonzalez, B. Leon, Structural study of sol-gel silicate glasses by IR and Raman spectroscopies, *J. Non-Cryst. Solids* 355 (8) (2009) 475–480, <https://doi.org/10.1016/j.jnoncrysol.2009.01.010>.
- [24] P. Innocenzi, Infrared spectroscopy of sol-gel derived silica-based films: a spectroscopic overview, *J. Non-Cryst. Solids* 316 (2003) 309–319, [https://doi.org/10.1016/S0022-3093\(02\)01637-X](https://doi.org/10.1016/S0022-3093(02)01637-X).
- [25] S. Raynaud, E. Champion, D. Bernache-Assollant, P. Thomas, Calcium phosphate apatites with variable Ca/P atomic ratio I. Synthesis, characterisation and thermal stability of powders, *Biomaterials* 23 (4) (2002) 1065–1072, [https://doi.org/10.1016/S0142-9612\(01\)00218-6](https://doi.org/10.1016/S0142-9612(01)00218-6).
- [26] R. Hussin, M.A. Salim, N.S. Alias, M.S. Abdullah, S. Abdullah, S.A.A. Fuzi, S. Hamdan, M.N. Md Yusof, Vibrational studies of calcium magnesium ultraphosphate glasses, *J. Fundamental Science* 5 (2009) 41–53, <https://doi.org/10.11113/mjfas.v5n1.286>.
- [27] P. Ros-Tàrraga, N.A. Mata, A. Murciano, P. Velasquez, P.N. De Aza, Multilayer materials: a method to link bioactivity and durability, *Ceram. Int.* 45 (17) (2019) 23611–23618, <https://doi.org/10.1016/j.ceramint.2019.08.072>.
- [28] T. Kasuga, Y. Ota, K. Tsji, Y. Abe, Preparation of High-strength calciumphosphate ceramics with low modulus of elasticity containing  $\beta$ -Ca(PO<sub>3</sub>)<sub>2</sub> fibers, *J. Am. Ceram. Soc.* 79 (7) (1996) 1821–1824, <https://doi.org/10.1111/j.1151-2916.1996.tb08001.x>.
- [29] W.L. Hill, G.T. Faust, D.S. Reynolds, The binary system P<sub>2</sub>O<sub>5</sub>-2CaO-P<sub>2</sub>O<sub>5</sub>, *Am. J. Sci.* 242 (9) (1944) 457–477, <https://doi.org/10.2475/ajs.242.9.457>.
- [30] Xi Wang, H.C. Schröder, W.E.G. Müller, Amorphous polyphosphate, a smart bioinspired nano-/bio-material for bone and cartilage regeneration: towards a new paradigm in tissue engineering, *J. Mater. Chem. B* 6 (2018) 2385–2412, <https://doi.org/10.1039/C8TB00241J>.
- [31] L.E. Rustom, M.J. Poellmann, A.J.W. Johnson, Mineralization in micropores of calcium phosphate scaffolds, *Acta Biomater.* 83 (2019) 435–455, <https://doi.org/10.1016/j.actbio.2018.11.003>.
- [32] J.R. Caeiro, P. Gonzalez, D. Guede, *Biomechanics and bone (& II): trials in different hierarchical levels of bone and alternative tools for the determination of bone strength*, *Rev. De Osteoporos. Metab. Miner.* 5 (2013) 99–108.
- [33] L.J. Gibson, M.F. Ashby, *Cellular Solids: Structure and Properties*, second ed., Pergamon, Oxford, 1999, pp. 429–452.
- [34] H. Zhou, S. Hou, M. Zhang, H. Chai, Y. Liu, S. B. Bhaduri, L. Yang, L. Deng, Synthesis of  $\beta$ -TCP and CPP containing biphasic calcium phosphates by a robust technique, *Ceram. Int.* 42 (2016) 11032–11038, <https://doi.org/10.1016/j.ceramint.2016.03.246>.
- [35] A. Yasukawa, S. Ouchi, K. Kandori, T. Ishikawa, Preparation and characterization of magnesium-calcium hydroxyapatites, *J. Mater. Chem.* 6 (1996) 1401–1405, <https://doi.org/10.1039/JM9606001401>.
- [36] F. Tamimi, D.L. Nihouannen, D.C. Bassett, S. Ibasco, U. Gbureck, J. Knowles, A. Wright, A. Flynn, S.V. Komarova, J.E. Barralet, Biocompatibility of magnesium

- phosphate minerals and their stability under physiological conditions, *Acta Biomater.* 7 (2011) 2678–2685, <https://doi.org/10.1016/j.actbio.2011.02.007>.
- [37] H. Zhou, S. Bhaduri, Novel microwave synthesis of amorphous calcium phosphate nanospheres, *J. Biomed. Mater. Res. B Appl. Biomater.* 100B (2012) 1142–1150, <https://doi.org/10.1002/jbm.b.32681>.
- [38] A.C. Tas, Submicron spheres of amorphous calcium phosphate forming in a stirred SBF solution at 55 °C, *J. Non-Cryst. Solids* 400 (2014) 27–32, <https://doi.org/10.1016/j.jnoncrysol.2014.04.031>.
- [39] H. Fleisch, R.G.G. Russell, S. Bisaz, P.A. Casey, R.C. Muehlbauer, The influence of pyrophosphate analogues (diphosphonates) on the precipitation and dissolution of calcium phosphate in vitro and in vivo, *Calcif. Tissue Res.* 2 (1968), 10–10A.
- [40] H. Fleisch, J. Maerki, R.G.G. Russell, Effect of pyrophosphate on dissolution of hydroxyapatite and its possible importance in calcium homeostasis, *Proc. Soc. Exp. Biol. Med.* 122 (1966) 317–320, <https://doi.org/10.3181/00379727-122-31123>.
- [41] A. Jung, S. Bisaz, P. Bartholdi, H. Fleisch, Influence of pyrophosphate on the exchange of calcium and phosphate ions on hydroxyapatite, *Calcif. Tissue Res.* 13 (1973) 27–40, <https://doi.org/10.1007/BF02015393>.
- [42] H. Gao, T. Tan, D. Wang, Dissolution mechanism and release kinetics of phosphate controlled release glasses in aqueous medium, *J. Contr. Release* 96 (2004) 29–36, <https://doi.org/10.1016/j.jconrel.2003.12.031>.
- [43] N.J. Lakkhar, I.H. Lee, H.W. Kim, V. Salih, I.B. Wall, J.C. Knowles, Bone formation controlled by biologically relevant inorganic ions: role and controlled delivery from phosphate-based glasses, *Adv. Drug Deliv. Rev.* 65 (4) (2013) 405–420, <https://doi.org/10.1016/j.addr.2012.05.015>.